



Effect of pre-stretching on the mechanical behaviour of three artificially aged 6xxx series aluminium alloys

Henrik Granum^{a,*}, Ole Runar Myhr^{a,b}, Tore Børvik^{a,c}, Odd Sture Hopperstad^{a,c}

^a Structural Impact Laboratory (SIMLab), Department of Structural Engineering, NTNU – Norwegian University of Science and Technology, Trondheim, Norway

^b Hydro Aluminium, Research and Technology Development, Sunndalsøra, Norway

^c Centre for Advanced Structural Analysis (CASA), NTNU, Trondheim, Norway

ARTICLE INFO

Keywords:

Pre-stretching
Crashworthiness
Aluminium alloys
Nanostructure model

ABSTRACT

The effect of pre-stretching on the mechanical behaviour of the aluminium alloys AA6063, AA6061 and AA6110 in temper T6 has been investigated. Uniaxial tensile tests and quasi-static axial crushing tests were conducted on rectangular hollow section (RHS) profiles pre-stretched 0.5 % and 4.0 % prior to artificial ageing. The stress-strain curves from the uniaxial tensile tests with different pre-stretching levels were used to investigate the effect of pre-stretching on the mechanical behaviour. It was found that the yield stress and ultimate tensile stress were somewhat lower and the failure strain was considerably higher for the profiles pre-stretched 4.0 % compared to those pre-stretched 0.5 %. In the crushing tests, less cracks were generally seen by visual inspection on the profiles pre-stretched 4.0 % but the specific energy absorption was slightly lower for these profiles. The nanostructure model NaMo was used to predict the stress-strain curves and the results were compared to the experimental data. Overall, the experimental trends were accurately predicted by NaMo, even though the hardening stagnation observed predominantly for profiles pre-stretched 4.0 % was not captured. The predicted evolution of the microstructure during artificial ageing was used to gain insight into the physical mechanisms responsible for the observed stress-strain behaviour.

1. Introduction

Aluminium alloys are used in numerous structural components designed for energy absorption, for instance crash management systems in vehicles [1]. The demand for increased performance and crashworthiness of safety components has led to extensive research activity on this topic during the last decades. In particular, the 6xxx series aluminium alloys have proved to satisfy most of the criteria wanted in safety components by combining high strength and ductility with excellent formability, surface quality and corrosion resistance. The automotive industry has been one of the leading industries to encourage innovations on these alloys, where the development of crashworthy and lightweight components is necessary to meet both environmental and safety requirements. The ongoing transition from a combustion engine to an electric motor in vehicles adds a new set of challenges the industry must overcome [2]. The safety of the passengers is no longer the only main priority in case of an accident, but also the battery pack must be sufficiently protected. Owing to the additional weight introduced by the battery pack and the structural complexity of the battery housing in an

electric vehicle, the current solutions may not be optimal. The development of aluminium alloys with enhanced mechanical properties is likely to play a major role in overcoming this challenge.

Since the first techniques to extract alumina emerged for over a century ago, researchers have experimented with aluminium as the main alloying element and invented new alloys with improved material properties. As a result of being employed in numerous industrial applications, aluminium alloys with tailored properties have been developed to meet requirements in the respective industries. However, altering the chemical composition of an alloy is not the only way to enhance the mechanical properties. Heat-treatment enhances properties like strength and work-hardening in aluminium alloys that respond to this process. Artificial ageing is the most effective process to increase the strength in age hardening alloys, such as the 6xxx series alloys considered here [3]. A heat-treatment then consists of two parts. First, the alloy is solution heat-treated at high temperature to dissolve the alloying elements followed by quenching to obtain supersaturation of these alloying elements. The alloy may then be stored at room temperature before it is subjected to artificial ageing where the strengthening precipitates form.

* Corresponding author.

E-mail address: henrik.granum@ntnu.no (H. Granum).

<https://doi.org/10.1016/j.mtcomm.2021.102408>

Received 14 December 2020; Received in revised form 19 April 2021; Accepted 28 April 2021

Available online 2 May 2021

2352-4928/© 2021 The Author(s). Published by Elsevier Ltd. This is an open access article under the CC BY license (<http://creativecommons.org/licenses/by/4.0/>).

Temper T6, usually denoted peak strength, is reached when an optimum combination of precipitates is present.

Aluminium extrusions are most often cold worked by stretching after extrusion to straighten the profiles and to reduce internal residual stresses that form during the extrusion and quenching process. The cold work is typically between 0.3 % and 1.0 % plastic strain and imposes negligible improvements of the mechanical properties in the subsequent heat-treatment according to Kaufman [4]. Stretching to higher pre-strains increases the dislocation density which provides sites for nucleation of precipitates in the subsequent artificial ageing.

Furu et al. [5] investigated the effect of pre-stretching on the aluminium alloys AA6005, AA6060 and AA6082. Rectangular profiles were extruded and pre-stretched 1.0 %, 5.0 % and 10.0 % before artificial ageing to three different temper conditions (underaged, peak aged and overaged). The experimental results revealed that there was a marked difference in the yield strength for various pre-stretching levels in all three alloys in the underaged temper. For the AA6005 pre-stretched 10.0 %, the yield stress was approximately doubled compared with the unstretched sample in the underaged temper. However, for the peak aged and overaged tempers, there were no prominent differences in the yield strength regardless of pre-stretching levels. In the peak aged condition, the amount of work-hardening decreased slightly for increasing levels of pre-stretching. The similar response between different levels of pre-stretching in the peak aged condition was attributed to an increased dislocation density that compensated for the decrease in the number density of β'' precipitates with increasing levels of pre-stretching.

A recent experimental study by Qvale et al. [6] on double-chamber extruded profiles made of the aluminium alloys AA6063 and AA6082 investigated the effect of pre-stretching on the microstructure and the mechanical behaviour. The study included uniaxial tensile tests, quasi-static and dynamic axial crushing tests and a transmission electron microscopy (TEM) study. The profiles were pre-stretched 0.5 % and 4.0 % after extrusion and prior to artificial ageing to temper T6. In the profiles pre-stretched 4.0 %, the length, cross-section and volume fraction of the precipitates were greater, while the number density was lower when compared to profiles pre-stretched 0.5 %. The uniaxial tensile tests revealed higher yield strength for AA6063 and lower yield strength for AA6082 in the 4.0 % pre-stretched condition when compared to corresponding alloys pre-stretched 0.5 %. The ultimate tensile strength was lower and the local failure strain higher in the 4.0 % pre-stretched materials compared to the 0.5 % pre-stretched materials. In the quasi-static and dynamic axial crushing experiments, a reduced amount of fracture was seen in the profiles pre-stretched 4.0 %, while the energy absorption was higher for AA6082 and lower for AA6063 when compared to corresponding profiles pre-stretched 0.5 %.

The effect of pre-stretching on the plasticity and fracture was investigated for AA6451-T4 aluminium sheets by Abi-Akl and Mohr [7]. Various material tests were conducted where selected specimens were pre-stretched 2.0 % and 5.0 %, followed by artificial ageing at 180 °C for 20 min for all specimens. Uniaxial tension tests in the rolling direction showed the same trends as reported by Furu et al. [5] for alloys in the underaged temper, namely that a higher level of pre-stretching gives a higher yield strength. Less work-hardening was observed for the highest level of pre-stretching and the ultimate tensile stress was reached at a lower plastic strain. Strain fields obtained by digital image correlation analyses indicated that the failure strain measured on the surface in various notch tension tests was lower for the highest level of pre-stretching.

Wang et al. [8] investigated a novel thermo-mechanical treatment that greatly improved the strength of an AA6061 aluminium sheet. The main steps in the process included underageing, cold rolling and re-ageing, where they were able to obtain a yield strength of 542 MPa and an ultimate tensile stress of 560 MPa for the alloy. The increased strength was addressed to a combination of precipitation hardening, dislocation strengthening, sub-structure strengthening and a high value

of the Taylor factor. The high strength obtained by this thermo-mechanical treatment is related to the extensive amount of cold work applied, in this case a reduction of the sheet thickness by 75 %. According to the strength-ductility trade-off [9], the ductility is expected to be significantly lower after this thermo-mechanical treatment than in the peak strength condition obtained by artificial ageing without the pre-deformation (temper T6), even though no local ductility measure was reported. In any case, these levels of cold work are not attainable for extrusions subjected to stretching before artificial ageing.

During the last decades, microstructure-based models able to predict the flow stress of aluminium alloys solely based on the chemical composition and thermo-mechanical treatment have emerged. Myhr and Grong [10] published a framework for modelling coupled nucleation, growth and coarsening in dilute alloys, which later became an integral part of the nanostructure model NaMo [11]. NaMo has received extensions to incorporate the effect of room temperature storage and cold deformation [12], and more recently the effect of strain rate and temperature [13]. Simar et al. [14] have published a microstructure-based framework able to predict the flow stress of precipitation hardening materials. The framework is based on the precipitation model by Myhr and Grong [10] and was used to predict the strength and strain hardening in friction stir welds of an AA6005-T6 aluminium alloy. A microstructure-based modelling framework that accounts for both isotropic and kinematic hardening contributions to the flow stress was presented by Fribourg et al. [15]. The framework was validated against an AA7449 aluminium alloy in various temper conditions and is based on the precipitation model by Simar et al. [14]. However, to the best of the authors' knowledge, NaMo is the only microstructure-based modelling framework for aluminium alloys that considers the effect of pre-stretching prior to artificial ageing.

In this study, the effect of pre-stretching on the mechanical behaviour of extruded rectangular hollow section (RHS) profiles made of three 6xxx series aluminium alloys, namely AA6063, AA6061 and AA6110, is examined. The main emphasis is on improving the ductility of the material by increasing the level of pre-stretching after extrusion. We build on the experimental study by Qvale et al. [6] and employ a similar thermo-mechanical treatment schedule, i.e., pre-stretching either 0.5 % or 4.0 % after extrusion and prior to artificial ageing to temper T6. Uniaxial tension tests and quasi-static axial crushing tests were conducted and the results were used to compare the effect of the pre-stretching in terms of the stress-strain curves in uniaxial tension, the force-displacement curves of the RHS profiles in axial folding, and the ductility of the material quantified by the strain to failure in uniaxial tension and the tendency for crack formation in axial folding. To describe the effect of pre-stretching, a novel extension to the equations controlling dynamic recovery in NaMo is proposed. Stress-strain curves predicted by NaMo were compared to the experimental data. The NaMo calculations were further used to gain insight into the differences in the microstructure of the 0.5 % and 4.0 % pre-stretched materials and to evaluate their influence on the stress-strain behaviour. The effects of pre-stretching on ductility are finally discussed considering recent results presented in the literature.

2. Materials and specimens

Three aluminium alloys provided by Hydro Aluminium were investigated in this study: AA6063, AA6061 and AA6110. The chemical composition of the alloys is given in Table 1. The aluminium alloys AA6063 and AA6061 are widely used crash alloys, expected to obtain a recrystallized grain structure after extrusion and quenching. AA6110 is an aluminium alloy with Mn and Cr added to facilitate the formation of dispersoids, resulting in a non-recrystallized grain structure. All materials were homogenized at 575 °C for 2 h and 15 min. Prior to extrusion, the billets were pre-heated to 500 °C and the extrusion process was according to the industrial guidelines for the given alloy. The alloys were extruded as RHS profiles with a cross-section of 37 mm × 29 mm and a

Table 1
Chemical composition of the aluminium alloys in wt-%.

	Si	Mg	Fe	Mn	Ti	Zn	Cu	Cr	Al
AA6063	0.512	0.470	0.206	0.047	0.006	0.003	0.001	0.001	Balance
AA6061	0.621	0.903	0.209	0.038	0.106	0.054	0.204	0.060	Balance
AA6110	0.720	0.828	0.196	0.506	0.026	0.003	0.203	0.157	Balance

wall thickness of 2.8 mm, see Fig. 1a). A casting length of approximately 1.5 m was used and after extrusion the profiles were water-quenched instantly. For a detailed description of the extrusion process, the reader is referred to Granum et al. [16]. Between 1 and 4 h after extrusion, the profiles were stretched in a Dartec servo-hydraulic universal testing machine either 0.5 % or 4.0 %, followed by 48 h storage at room temperature. All profiles were then heat-treated at 185°C for 8 h to obtain temper T6 (peak strength). The profiles were cut into lengths of 100 mm before a geometrical trigger for the axial crushing tests was machined according to Fig. 1a) by means of wire erosion. A micrometre was used to measure the thickness of the four walls and all profiles were weighed prior to testing.

3. Tensile tests

Uniaxial tension (UT60) specimens were cut from each of the four walls of the profiles along the extrusion direction. The geometry of the specimen is given in Fig. 1b). Longitudinal weld seams created during the extrusion in the middle of each wall are marked with blue wavy lines in Fig. 1a). The specimens were cut such that the extrusion weld was present in the specimen taken from the narrow sides, while it was absent in the specimens taken from the wide sides, as depicted in the figure. The thickness of the specimens was measured in the gauge region prior to testing and the average wall thickness was 2.758 mm and 2.656 mm for profiles pre-stretched 0.5 % and 4.0 %, respectively. An Instron 5985 universal testing machine was used to carry out the uniaxial tensile tests. The tests were conducted at ambient temperature with an initial strain rate of $5 \times 10^{-4} \text{ s}^{-1}$. Before testing, the specimens were spray-painted with a speckle pattern to enable digital image correlation (2D-DIC). A Prosilica GC2450 digital camera oriented perpendicularly to the in-plane specimen surface captured images with a resolution of $2448 \times$

802 pixels at 1 Hz. A 30 kN load-cell attached to the machine measured the force, also at 1 Hz. 2D-DIC analyses were conducted with the in-house software eCorr [17], applying a mesh of square elements. The characteristic element length was 25 pixels or just above 0.4 mm. A 17.5 mm long virtual extensometer placed symmetrically with respect to the centre of the gauge region was used to extract displacements from the tests.

Engineering stress-strain curves to fracture and true stress-strain curves to necking for all tensile tests are shown in Fig. 2a) and b), respectively. A total of four tests were conducted per material, i.e., one specimen from each wall of the profile. The solid and dashed curves represent tests of profiles pre-stretched 0.5 % and 4.0 %, respectively. To distinguish between the two conditions, the labels “–0.5 %” and “–4.0 %” were appended to the alloy designation to represent the profiles pre-stretched 0.5 % and 4.0 %, respectively. By inspection of Fig. 2, AA6110 has the highest yield strength, closely followed by AA6061, while AA6063 has a significantly lower yield strength. The yield strength was slightly affected by the 4.0 % pre-stretching, but within the scatter of the measured stress data for AA6110 and AA6061. The difference was more prominent for AA6063, yet below 10 MPa. As a result, the AA6063–4.0 % curves were shifted downwards compared to the AA6063–0.5 % curves all the way to fracture. The tensile tests of specimens taken from profiles pre-stretched 4.0 % exhibited lower work-hardening than the ones pre-stretched 0.5 %, particularly for AA6061 and AA6063. As a result, diffuse necking was reached for a lower strain in the alloys pre-stretched 4.0 % compared to those pre-stretched 0.5 %, see Fig. 2b). The earlier necking of the materials pre-stretched 4.0 % is also evident from the engineering stress-strain curves in Fig. 2a). The AA6110 curves were seen to pair up, dependent on whether the extrusion weld was present in the gauge area or not. In the test specimens where the extrusion weld was present, the yield stress was approximately 6 MPa

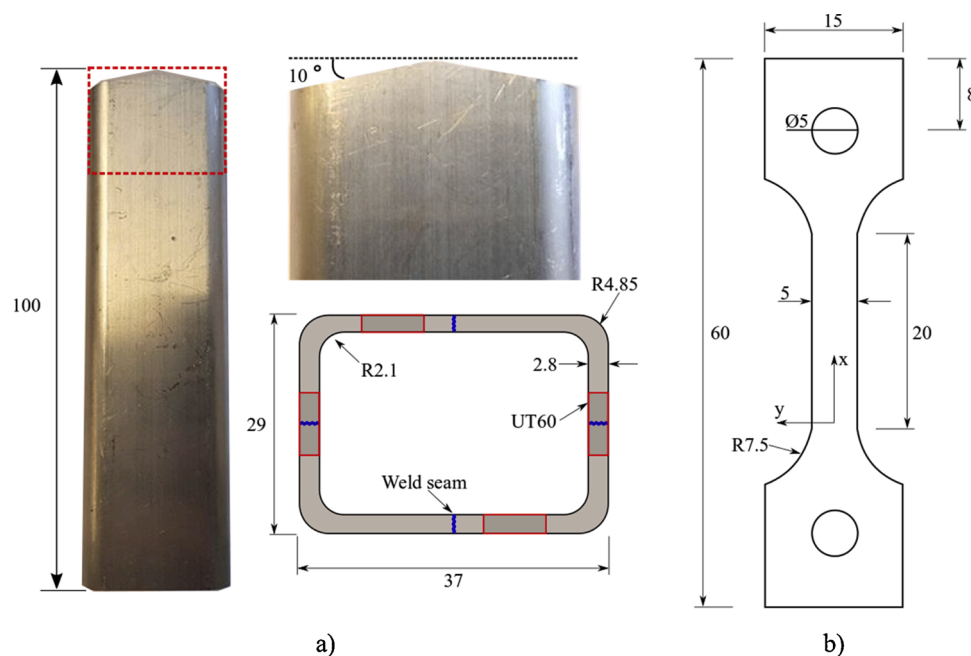


Fig. 1. Nominal dimensions of a) axial crushing test specimens with geometrical trigger and b) uniaxial tension (UT60) specimen. All measures are in mm. The positions of the UT60 specimens and the four weld seams are shown on the cross-section of the extruded profile.

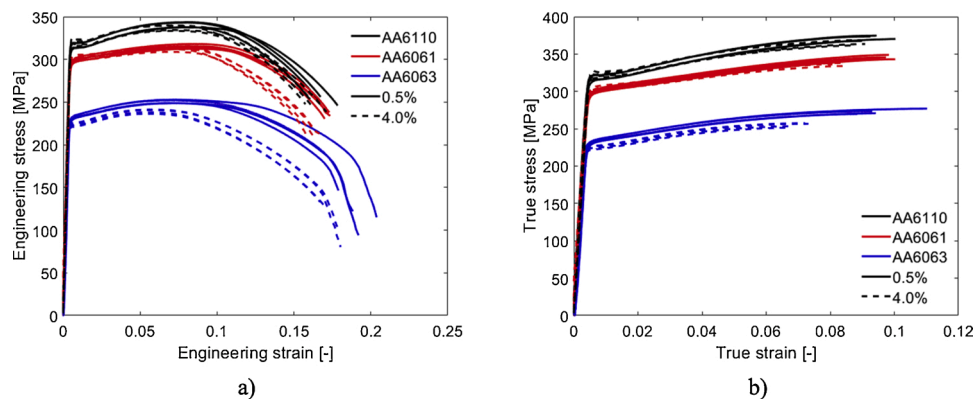


Fig. 2. a) Engineering stress-strain curves from all tensile tests to fracture and b) true stress-strain curves to necking.

lower than in the specimens without an extrusion weld. The differences in the mechanical properties related to the presence of an extrusion weld was not investigated any further in this study and representative tests were chosen from specimens without a weld seam.

In particular, the AA6110–0.5 % and AA6110–4.0 % curves exhibit a distinct yield plateau, but also the AA6061–4.0 % and AA6063–4.0 % curves show signs of a yield plateau, though less pronounced. The differences in the work-hardening behaviour of the materials are more readily analysed by use of work-hardening rate vs. equivalent plastic strain plots shown in Fig. 3. To ensure informative results, a curve-fit of the true stress-strain curve up to necking was conducted in MATLAB. A Gaussian function was used to ensure a good fit with the experimental data, and the R-squared value was above 0.99 for all curve fits. Fig. 3 shows that hardening stagnation is present for all materials, but to a greater extent for AA6110 than for AA6061 and AA6063, and for the materials pre-stretched 4.0 % than for those pre-stretched 0.5 %.

By use of 2D-DIC, the major principal strain field $\epsilon_1(x,y)$ can be calculated as a function of the overall straining of the specimen, where x and y are the coordinates in the extrusion and transverse directions, respectively, see Fig. 1b). In Fig. 4, the principal strain $\epsilon_1(x,0)$ along the centre line of the gauge region for representative tests is plotted as a function of frame number. The surface plots reveal that the major principal strain ϵ_1 is reasonably uniformly distributed over the gauge region before plastic instability (or necking) leads to rapid growth of ϵ_1 at the position of the neck. By comparing the values of the major principal strain at failure, it is evident that the specimens pre-stretched 4.0 % exhibit larger values than those pre-stretched 0.5 %. The proof stress at 0.2 % plastic strain $\sigma_{0.2}$, the ultimate tensile strength σ_u and the major principal strain at failure ϵ_f from representative tests are presented in

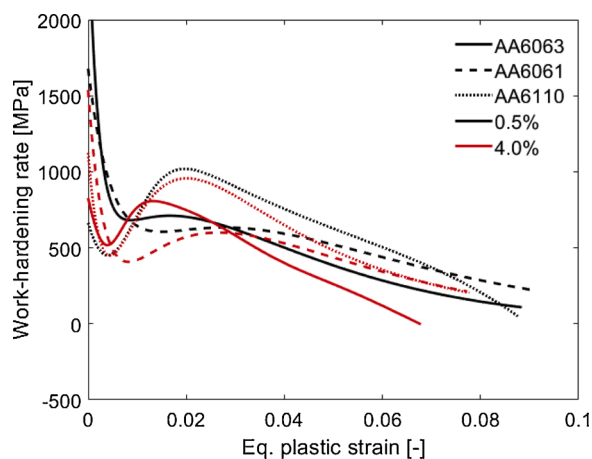


Fig. 3. Work-hardening rate vs. equivalent plastic strain plots for all materials based on the representative tests.

Table 2. The failure strain ϵ_f was found by examining the strains in all elements within the neck at failure and selecting the largest value. The effect of offsetting the mesh was investigated and used to avoid potential spurious output [6]. The superior ductility of the specimens pre-stretched 4.0 % is evident, where the failure strain is between 17 % and 19 % higher compared to the ones pre-stretched 0.5 %. However, this method to determine the failure strain is prone to noise and the reported values should be interpreted as estimates.

The representative test of the AA6110–4.0 % material was investigated further due to the prominent yield plateau exhibited in this test. To visualize the phenomenon occurring at yield, the strain rate was estimated as the increment of the major principal strain divided by the time increment. A plot of the strain rate as a function of gauge position and frame number is shown in Fig. 5, also showing the engineering stress as a function of the frame number. It is evident that a band of elevated strain rate travels across the gauge section with approximately constant velocity, starting after the specimen yields. Only one band is seen, and the material starts to work-harden only after the band arrives at the end. The band propagation is similar to the behaviour of Lüders band found in low-carbon steels and Al-Mg alloys, but the relatively low Mg content in the AA6110 alloy and the artificial ageing suggest that the underlying physical mechanism is different.

4. Axial crushing tests

The quasi-static axial crushing tests were conducted in an Instron 5985-series universal testing machine at ambient temperature. The results of the profiles pre-stretched 0.5 % have already been presented in Granum et al. [16], but are included for the completeness of the study. The specimen geometry is shown in Fig. 1a), where a geometrical trigger is used to control the initiation of the folding process. A constant velocity of 30 mm/min was prescribed to the crosshead of the test machine and the test was stopped when the profiles were deformed 67 mm. Two cameras captured the deformation at 5 fps from two different angles with a resolution of 2448×1600 pixels. The axial force and displacement were recorded at 5 fps by a 250 kN load-cell attached to the machine, synchronized with the images. The profiles were placed directly on the level steel platen below the load cell, and no effort was made to constrain the profiles during deformation. Three tests for each material combination were conducted, resulting in a total of 18 crushing tests.

The force-displacement curves are displayed in Fig. 6 along with mean force curves for all component tests. The repeatability between duplicate tests is excellent owing to the geometrical trigger, which ensures that the deformation initiates at the top of the profile. The most notable discrepancy between repeat tests is seen for AA6061–4.0% where one of the tests exhibits a slightly different folding mode after the first peak. The force-displacement curves have four main peaks except for AA6110, where also a minor peak after the first one is seen. Each of the main peaks correlates to a fold in the deformed profile. The profiles

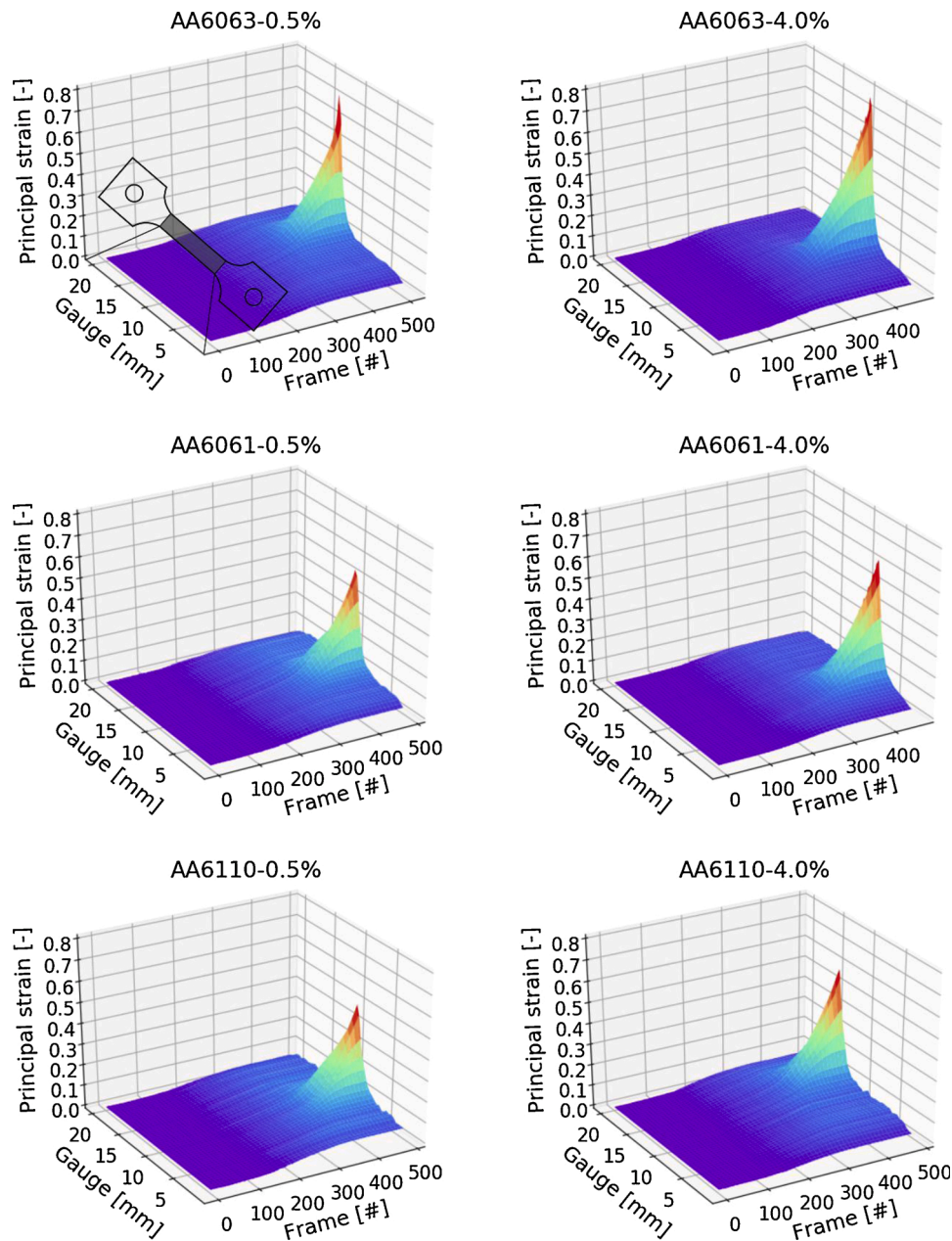


Fig. 4. Surface plots of the major principal strain along the centre line of the gauge region for representative tests plotted as a function of frame number.

Table 2

Material properties from representative tests: proof stress at 0.2 % plastic strain $\sigma_{0.2}$, ultimate tensile strength σ_u and the major principal strain at failure ϵ_f .

Alloy	Pre-stretch	$\sigma_{0.2}$ [MPa]	σ_u [MPa]	ϵ_f [-]
AA6063	0.5 %	230	274	0.79
	4.0 %	224	257	0.94
AA6061	0.5 %	300	346	0.59
	4.0 %	303	338	0.69
AA6110	0.5 %	320	374	0.55
	4.0 %	322	367	0.65

pre-stretched 4.0 % display slightly lower force levels throughout the deformation, clearly visualized by the mean force curves. The lower mean force levels are partly related to the thinner wall thickness of the profiles pre-stretched 4.0 %. To assess the crashworthiness of profiles with different pre-stretch levels and enable a direct comparison, the specific mean force, i.e., the mean force divided by the average mass,

was calculated for all cases, see Table 3. The material with the highest specific energy absorption capability is AA6110–0.5 % followed by AA6061–0.5 %. However, AA6110–4.0 % and AA6061–4.0 % follow closely after. AA6063–0.5 % and AA6063–4.0 % have in turn 22 % and 24 % lower specific energy absorption than AA6110–0.5 %. This is approximately the same percentage difference as seen in the yield stress and the ultimate tensile strength between these alloys. The profiles pre-stretched 4.0 % exhibit consistently lower specific mean force values than corresponding profiles pre-stretched 0.5 %. As there are only small differences in the yield strength of an alloy pre-stretched 0.5 % and 4.0 %, the variations in specific mean force are likely related to differences in the work-hardening and the ultimate tensile strength. The profiles pre-stretched 4.0 % exhibit lower work-hardening capacity than profiles pre-stretched 0.5 %, as illustrated in Fig. 3. Overall, the trends in the resulting mean forces agree with the engineering stress-strain curves in Fig. 2a), in the sense that a high/low engineering stress level leads to a high/low mean force.

Deformed profiles from representative tests are shown in Fig. 7. The

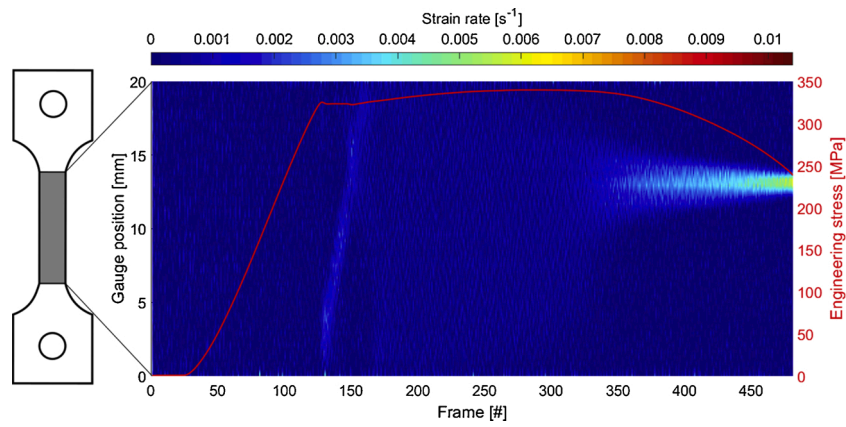


Fig. 5. Plot of the strain rate as a function of gauge position and frame number along with the engineering stress plotted against the frame number. The colour bar indicates the strain rate level.

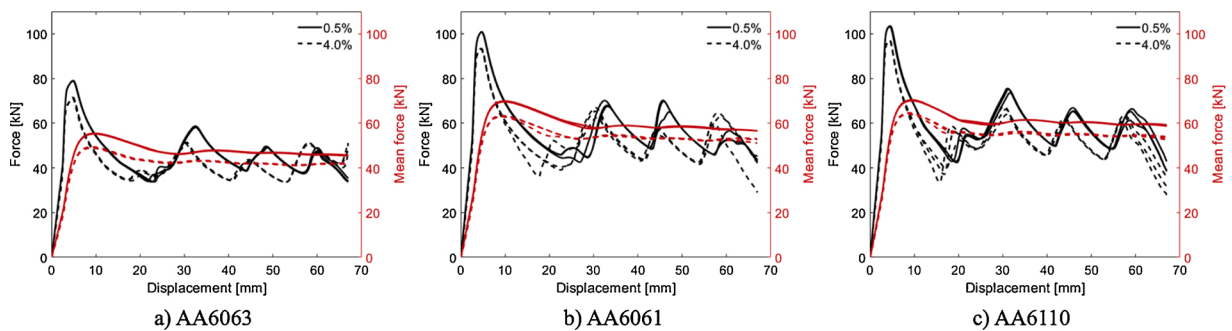


Fig. 6. Force-displacement curves and mean force-displacement curves from the axial crushing tests: a) AA6063, b) AA6061 and c) AA6110.

Table 3

Average mass and specific mean force (i.e., mean force divided by mass) for all alloy and pre-stretch combinations.

	0.5 % pre-stretch			4.0 % pre-stretch		
	Mass [g]	Specific mean force [N/g]	Cracks i = internal e = external	Mass [g]	Specific mean force [N/g]	Cracks i = internal e = external
AA6063	84.13	540.5	Yes (i)	79.39	528.8	No
AA6061	84.25	670.8	Yes (i,e)	79.07	660.8	Yes (i)
AA6110	84.55	696.4	Yes (i,e)	80.02	667.8	Yes (i)

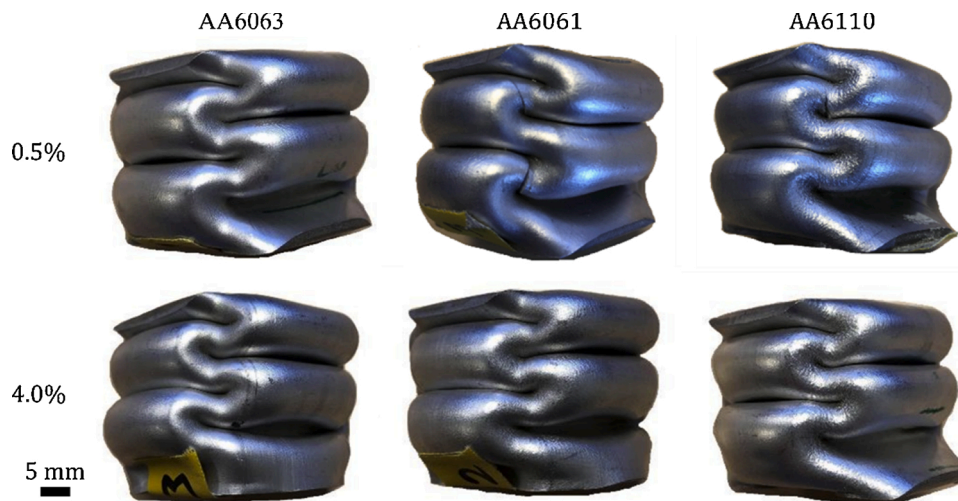


Fig. 7. Deformed profiles from representative tests of all alloy and pre-stretch combinations.

folding pattern is similar in all tests, thus independent of the alloy and pre-stretch combination. By inspection of the deformed profiles, cracks are seen in the folds of the AA6061–0.5 % and AA6110–0.5 % profiles. However, the cracks are not found to substantially influence the crushing performance because the folding pattern is similar for an alloy pre-stretched 0.5 % and 4.0 %. The cracks are not found to substantially influence the force-displacement curves either, since the differences between pre-stretch levels are mainly attributed to the different wall thicknesses. Overall, no cracks were seen by visual inspection on the exterior of any of the profiles pre-stretched 4.0 % or any of the AA6063–0.5 % profiles. The surfaces of the folded profiles pre-stretched 4.0 % were smooth and showed no signs of incipient damage, apart from the AA6110 profiles that had developed orange peeling in the folds. The bottom part of the AA6063–4.0 % profile was not seen to slide out as in the other tests, which resulted in an increase in the force at the end of the force-displacement curves in Fig. 6a). As a result, the folds are slightly more compressed compared to the other alloy and pre-stretch combinations.

To reveal the degree of damage in the interior of the profiles, a deformed profile from each alloy and pre-stretch combination was cut in half. These are shown in Fig. 8, where red circles indicate the locations of incipient cracks. Although the exterior of the profile showed no signs of incipient cracks, the interior may have cracks present. For the AA6063–0.5% profile, a small incipient crack is seen in a fold, apparently barely penetrating the surface. The rest of the profile shows no sign of cracks. The AA6063–4.0% profile, on the other hand, shows no sign of cracks and has smooth surfaces in all folds. The AA6061–0.5% profile has both incipient and through-thickness cracks in the interior. However, the cracks are not necessarily located in the same place as the cracks found on the exterior of the profile. Three minor incipient cracks are seen in the top fold of the AA6061–4.0% profile. The AA6110–0.5% profile has some prominent cracks which apparently extend through the thickness, as the positions of the cracks correspond with the ones on the exterior. The AA6110–4.0% profile has incipient cracks in the same part of the folds as the AA6110–0.5% profile, but to a lesser extent. Overall, the same trend as seen on the exterior of the profiles is seen in the interior, where profiles pre-stretched 4.0 % show considerably lower degree of cracking than those pre-stretched 0.5 %. Interestingly, the interior of the profiles reveals a higher degree of cracking than the exterior, suggesting that the interior is more susceptible to crack initiation. It is reasonable to believe that the degree of cracking seen for the AA6110 profiles is among others linked to the formation of orange peeling on the surfaces, as the degree of cracking is more prominent than for the AA6061 profiles.

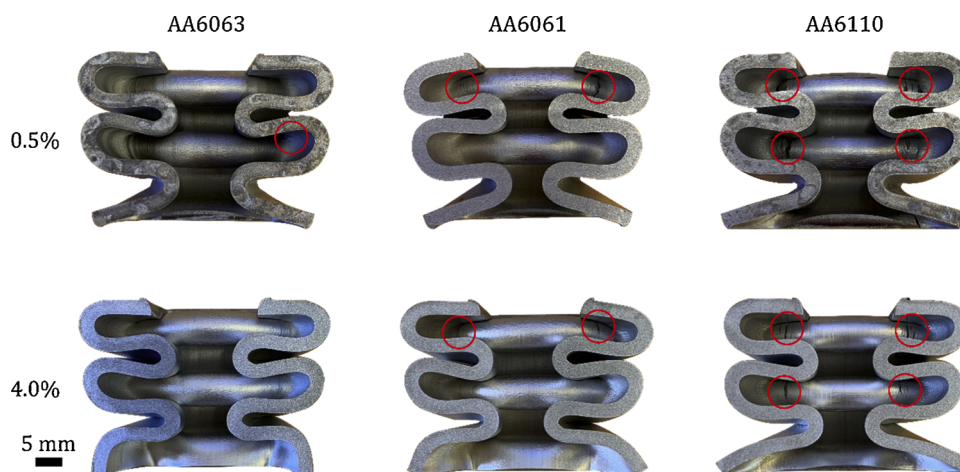


Fig. 8. Interior of the deformed profiles of all alloy and pre-stretch combinations. The locations of the cracks are indicated by the red circles (For interpretation of the references to colour in this figure legend, the reader is referred to the web version of this article).

5. Nanostructure model (NaMo)

A combined precipitation, yield strength and work-hardening model for Al-Mg-Si alloys, denoted NaMo, is used to predict the stress-strain behaviour of the alloys in this study. The layout and interaction of the sub-models of NaMo are depicted in Fig. 9. The figure shows how parameters related to the precipitates and dislocations are transferred between the sub-models. In the precipitation model, the number of particles N_i within the discrete radius class r_i is calculated. From the precipitation model the effective solid solution concentration C_{ss} , the volume fraction of non-shearable particles f_0 , and the geometric slip distance λ_g are predicted and transferred to the work-hardening model. In the work-hardening model, the evolution of the dislocation density ρ is predicted as a function of plastic strain p and transferred to the precipitation model and yield stress model. The yield stress model receives the mean planar spacing between particles in the slip plane along the bending dislocation l , the mean interaction force between particles and dislocations \bar{F} , and the predicted concentration of an element in solid solution C_i with i equal to Mg, Si, Cu and Mn from the precipitation model. Finally, the yield stress σ_y (or the flow stress) as a function of the plastic strain p is predicted. An extensive description of the sub-models of NaMo together with the complete mathematical framework can be found in [11–13]. In this section, a presentation of the most important ingredients of NaMo is given. As the work-hardening model was slightly revised in conjunction with this study, this sub-model is presented in detail.

The objective of the precipitation model is to calculate the evolution of the particle size distributions (PSDs) during the different time steps of the thermo-mechanical process the material undergoes. The current model calculates two individual PSDs, one for atomic clusters and one for metastable β'' and β' particles. The model is based on the Kampmann-Wagner formalism [18] and has three main components: nucleation laws that predict the number of stable nuclei that form at each time step, rate laws that calculate either the dissolution or the growth rate of particles within each discrete size class, and a continuity equation that keeps record of the amount of solute being tied up in the precipitated hardening particles. Natural ageing (i.e., ageing at room temperature) is accounted for by the PSD for cluster evolution. During the subsequent artificial ageing, there is a complex interplay between the two PSDs as the clusters, which are not stable at elevated temperatures, gradually tend to dissolve, at the same time as β'' and β' particles precipitate [12]. These two PSDs contain individual nucleation and rate laws but are linked together by the continuity equation.

As illustrated in Fig. 9, key parameters are extracted from the PSDs and used as inputs to the yield strength model, where the strength

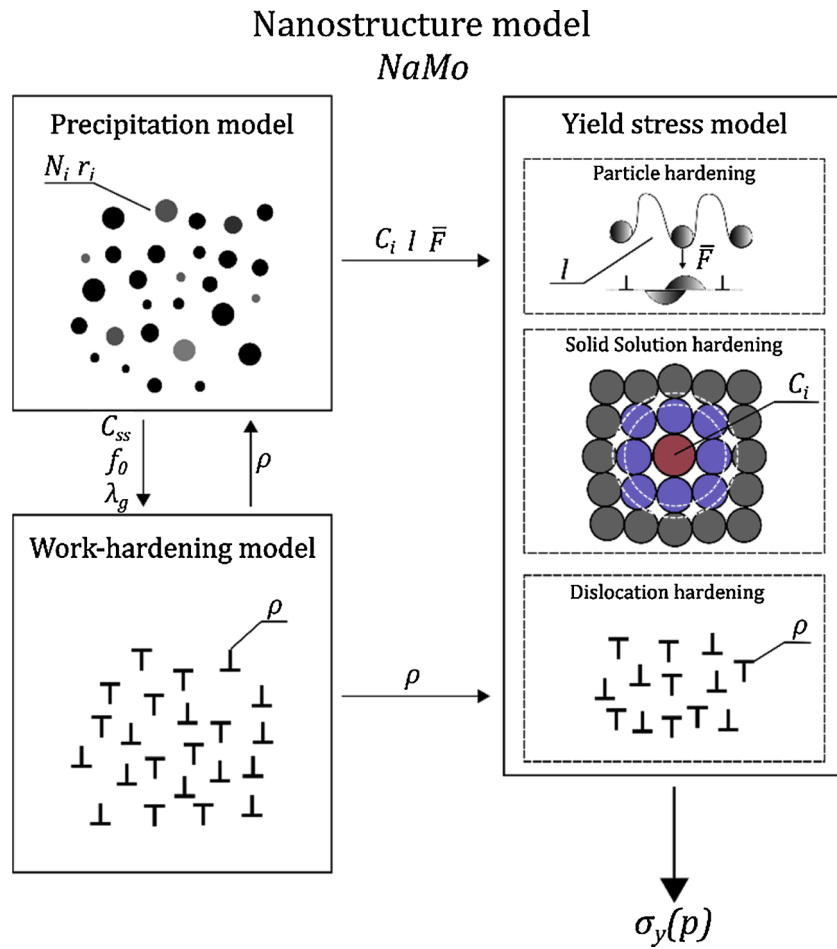


Fig. 9. Outline of NaMo with coupling between the various sub-models. The parameters and symbols in the figure are explained in the text.

contributions are added linearly as follows:

$$\sigma_y = \sigma_i + \sigma_{ss} + \sigma_p + \sigma_d \quad (1)$$

Here, σ_y is the yield stress of the alloy, σ_i is the intrinsic yield strength of pure aluminium, σ_{ss} is the contribution from elements in solid solution, σ_p is the contribution from precipitates and clusters, and σ_d is the contribution from dislocations. The yield stress σ_y depends on the plastic strain p and thus represents the flow stress of the material during plastic deformation. The effect of grain size strengthening is omitted in this model, considering that the contribution from the Hall-Petch effect is relatively small compared with the other strength contributions for the present type of alloys and heat treatment schedules [19].

The contribution from elements in solid solution to the yield stress, σ_{ss} , is calculated as

$$\sigma_{ss} = \sum_i k_i C_i^{2/3} \quad (2)$$

where C_i is the concentration of a specific element in solid solution and k_i is the corresponding scaling factor with i equal to Mg, Si, Cu and Mn. The concentrations of Mg and Si vary during a heat-treatment, as calculated by the precipitation model from the predicted PSDs at each time step. From the PSDs the volume fractions of clusters and hardening particles can be estimated. The volume fractions are used to predict the resulting concentrations of Mg and Si from the continuity equation.

The strength contribution from precipitates and clusters, σ_p , is given as

$$\sigma_p = \sqrt{\sigma_{p1}^2 + \sigma_{p2}^2} = \sqrt{\left(\frac{M\bar{F}_1}{bl_1}\right)^2 + \left(\frac{M\bar{F}_2}{bl_2}\right)^2} \quad (3)$$

where M is the Taylor factor, b is the magnitude of the Burgers vector, \bar{F}_1 and \bar{F}_2 are the mean obstacle strengths for the two PSDs, and l_1 and l_2 are the effective particle spacing in the slip plane along the bending dislocation for the two PSDs. The parameters \bar{F}_i and l_i ($i = 1, 2$) are calculated by the precipitation model in a similar way for clusters and precipitates.

The final term in Eq. (1), σ_d , represents the contribution from dislocations to the yield stress as calculated based on results from the work-hardening model. The model calculates the total dislocation density ρ , which is assumed to be the sum of statistically stored dislocations (SSDs), ρ_s , and geometrically necessary dislocations (GNDs), ρ_g . The dislocation densities ρ_s and ρ_g are calculated by evolution laws that will be explained in the following. The contribution from the dislocations is given as

$$\sigma_d = \alpha M \mu b \sqrt{\rho_s + \rho_g} \quad (4)$$

where α is a constant with value close to 0.3 and μ is the shear modulus.

The work hardening model is coupled with the precipitation model to account for the gradual transition from matrix nucleation of β'' particles to nucleation of β' particles along dislocation lines for increasing ρ_s as observed in several TEM investigations [20,21]. The evolution of ρ_s is governed by a Kocks-Mecking type of relationship. In the present work, this expression is slightly modified in order to account for pre-stretching of the alloy prior to the artificial ageing. It is assumed that the SSDs that

act as nucleation sites for β' particles are locked and will not be subjected to dynamic recovery during the final deformation. If the density of locked dislocations after pre-stretching and artificial ageing is denoted ρ_s^* , then a reasonable modification of the Kocks-Mecking equation is

$$\frac{d\rho_s}{dp} = k_1\sqrt{\rho_s} - k_2(\rho_s - \rho_s^*) \quad (5)$$

Here, k_1 is a constant characteristic for the material, k_2 is a parameter that controls the rate of dynamic recovery during plastic deformation, while ρ_s^* is estimated as

$$\rho_s^* = \rho_s(t^*)\phi(t^*) \quad (6)$$

where t^* is the point in time when the final deformation starts, and the factor ϕ is an estimate on the number density of SSDs that are locked at the start of the final deformation relative to the total number density of SSDs. Further, ϕ is estimated based on the integrated number of nucleated β'' and β' particles as follows

$$\phi(t) = \frac{\int_0^t j_{\beta'} d\bar{t}}{\int_0^t j_{\beta'} d\bar{t} + \int_0^t j_{\beta''} d\bar{t}} \quad (7)$$

where $j_{\beta'}$ and $j_{\beta''}$ are the nucleation rates for β' and β'' particles, respectively.

The effect of elements in solid solution on the dynamic recovery is accounted for by defining the dynamic recovery coefficient k_2 by

$$k_2 = k_1 \frac{\alpha M \mu b}{k_3 (C_{ss})^{3/4}} \quad (8)$$

Here, k_3 is a parameter governing the influence of solutes and C_{ss} is an effective solid solution concentration which includes a weighted overall effect of Mg and Si in solid solution [11]. According to Eq. (8), k_2 may increase to very large values as C_{ss} approaches zero. This is probably not realistic, as the corresponding dynamic recovery rate gives practically no work hardening when C_{ss} becomes sufficiently small. Hence, in the present work, an upper limit to k_2 is introduced. This value is hard to define, but a rough estimate based on observed work-hardening rates for some low alloyed 6xxx series aluminium alloys indicates an upper value of about 60 (e.g., [22]), which has been used for the simulations in the present work.

During pre-stretching prior to artificial ageing, the alloying elements are predominantly in solid solution, thus the imposed plastic strain will increase the number density of the SSDs, ρ_s , according to Eq. (5). In the subsequent artificial ageing, the dislocation density generated by the pre-stretching may decrease due to static recovery processes taking place at elevated temperatures. The expression for static recovery incorporates annihilation of dislocations and is given on rate form as [23–25]

$$\frac{d\rho}{dt} = -k_4 \rho^{3/2} \exp\left(-\frac{U_s}{RT}\right) \sinh\left(\frac{k_5 \sqrt{\rho}}{RT}\right) \quad (9)$$

where U_s is the average activation energy for the solute diffusion obstructing the dislocation movement, R is the universal gas constant (8.314 J/Kmol), T is the temperature, while k_4 and k_5 are model parameters adopted from Furu et al. [5].

The evolution rule for the density of GNDs is given as [13]

$$\frac{d\rho_g}{dp} = \frac{k_{1g}}{\lambda_g} - k_{2g}\rho_g \quad (10)$$

where k_{1g} governs the storage rate of GNDs and λ_g is the geometric slip distance, which describes the effectiveness of non-shearable hardening particles to store dislocations during plastic deformation. The dynamic recovery constant k_{2g} in the evolution rule for ρ_g is given by [13]

$$k_{2g} = k_{2g}^{\text{ref}} \left(\frac{f_0}{f_0^{\text{ref}}}\right) \quad (11)$$

where f_0 and f_0^{ref} are volume fractions of non-shearable particles in the current material and a reference material, respectively, and k_{2g}^{ref} is the dynamic recovery constant of the reference material. The precipitation model calculates the number density and radius of the particles, where the ones with a radius above a critical limit are considered non-shearable. The geometric slip distance is calculated as [11]

$$\lambda_g = \left(8 \sum_{r_i=r_c}^{r_i=\infty} r_i^2 N_i\right)^{-1} \quad (12)$$

where r_i is the size class of the particles and N_i is the number of particles per unit volume within this class. The critical radius of the particle is denoted r_c . The volume fraction of non-shearable particles is calculated as [11]

$$f_0 = \sum_{r_i=r_c}^{r_i=\infty} \frac{4}{3} \pi r_i^3 N_i \quad (13)$$

The reader is referred to References [11–13] for further details on the nanostructure model NaMo and the calibration and validation of the model against experimental data. The inputs to the model are the chemical composition of the alloy and its thermo-mechanical history. In the subsequent simulations with NaMo, parameter values determined in the studies [11–13] have been used with no further calibration to the experimental data. The only new parameter is the upper limit to the dynamic recovery coefficient k_2 entering the evolution rule for the SSDs.

6. Numerical results and discussion

The flow stress curves up to necking from the tensile tests in terms of true stress and equivalent plastic strain are shown in Fig. 10a). The corresponding flow stress curves predicted by NaMo, based on the chemical composition and the thermo-mechanical history (i.e., pre-stretching, artificial ageing and final stretching) of the material, are shown in Fig. 10b). The yield strength predictions are in reasonable agreement with the experimental results, but the predicted values are somewhat high for AA6110–0.5%, AA6110–4.0% and AA6063–4.0%. Also, the yield strength of AA6063–4.0% is predicted to be slightly higher than the yield strength of AA6063–0.5%, whereas the opposite is seen in the experiments. Overall, the trends in the work-hardening are correctly predicted, where a slightly lower work-hardening is obtained for 4.0 % pre-stretching than for 0.5 % pre-stretching. However, the hardening stagnation observed for all materials, but to a higher degree for those pre-stretched 4.0 %, is not captured by NaMo.

To better understand the differences between the stress-strain curves predicted by NaMo for the two levels of pre-stretching, the evolution of parameters governing the microstructure is investigated. Previously, the predictions by NaMo have been compared to results from TEM-studies, see e.g., [12,26,27], for a variety of 6xxx series aluminium alloys. In general, good agreement between the precipitation parameters predicted by NaMo and the ones measured by TEM has been found, e.g., for AA6063 in [27]. The evolution of selected parameters during artificial ageing for AA6061 pre-stretched 0.5 % and 4.0 % is shown in Fig. 11.

The evolution of the dynamic recovery parameter, k_2 , in Fig. 11a) demonstrates an increase from the initial value of around 20 to the upper limit of 60 for both pre-stretch levels. The difference in dynamic recovery between the two pre-stretch levels is then predominantly due to the differences in ρ_s and ρ_s^* , according to Eq. (5).

The effective solid solution concentration, C_{ss} , is seen in Fig. 11b) to decrease for both pre-stretch levels during artificial ageing; the final value being somewhat lower for the 4.0 % pre-stretched alloy. The decrease of C_{ss} is caused by solute being tied up in clusters that form

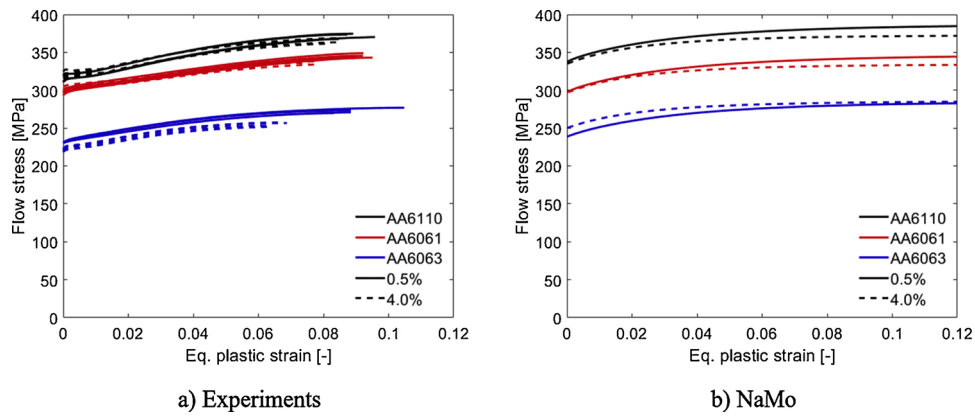


Fig. 10. Comparison between measured and predicted flow stress curves for the different alloys and pre-stretching conditions: (a) experiments and (b) NaMo predictions.

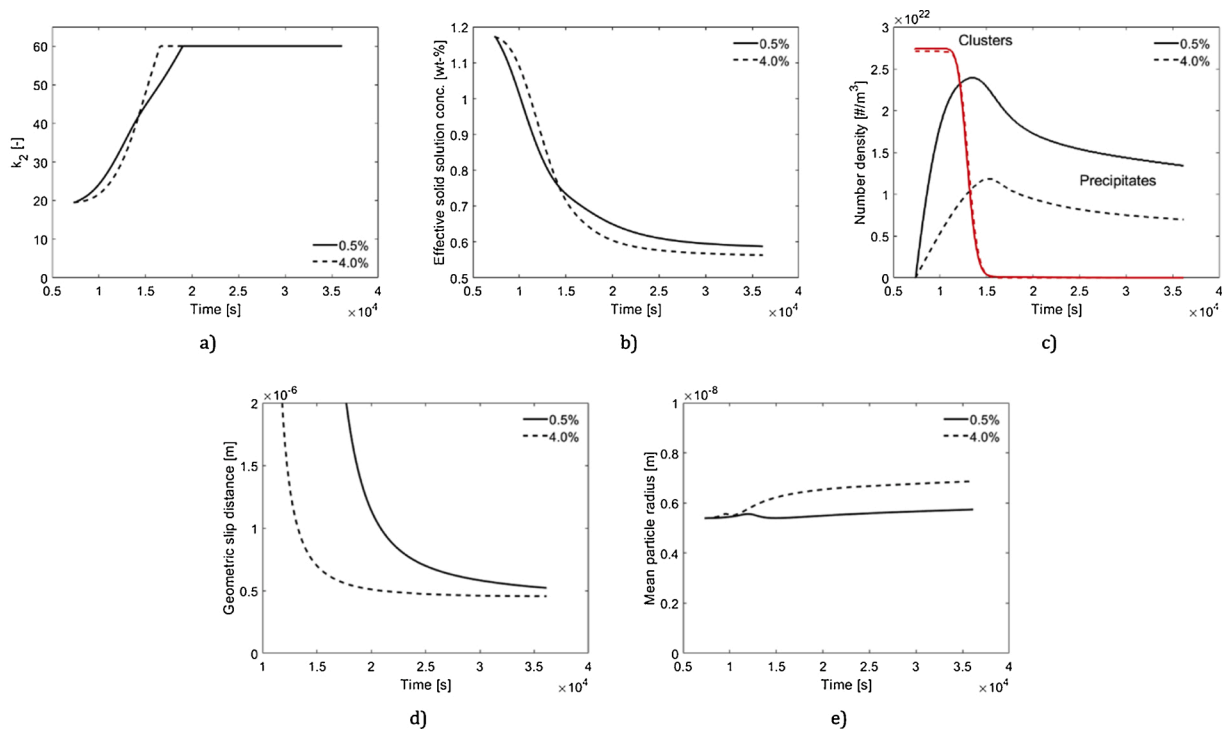


Fig. 11. Evolution of selected parameters for AA6061 pre-stretched 0.5 % and 4.0 % during the artificial ageing as predicted by NaMo: a) dynamic recovery parameter, k_2 , b) effective solid solution concentration, C_{ss} , c) number density of clusters and precipitates, d) geometric slip distance of non-shearable particles, λ_g , and e) mean radius of non-shearable particles.

during the natural ageing and precipitates that form during the subsequent artificial ageing. At the early stage of the artificial ageing, there is a complex interplay between clusters that dissolve and precipitates that nucleate and grow. The overall effect is a gradual decrease in the effective solid solution concentration C_{ss} during the artificial ageing, as shown in Fig. 11b). According to Eq. (8), a lower value of C_{ss} increases the dynamic recovery by increasing the value of k_2 . The result is that dislocations stored during pre-stretching that were not pinned by β' particles would become unstable during plastic straining after the artificial ageing. As will be discussed below, this could be the physical mechanism behind the work-hardening stagnation seen to various degrees for all the tested materials.

The evolution of the number density of clusters and precipitates is shown in Fig. 11c). The clusters that formed during natural ageing dissolve as precipitates form during the artificial ageing. The 0.5 % pre-stretched alloy is seen to nucleate a markedly higher number density of

precipitates than the 4.0 % pre-stretched alloy, where the final values are somewhat lower compared to the peak values for both pre-stretch levels. The difference in number density of precipitates is linked to the conjecture that larger β' precipitates nucleate along dislocation lines in the 4.0 % pre-stretched material, whereas in the 0.5 % pre-stretched material, the majority of precipitates is smaller β'' precipitates that nucleate in the bulk. The precipitates contribute to the yield strength according to Eq. (3), where the mean obstacle strength, \bar{F} , and the mean effective particle spacing, l , are parameters calculated by the precipitation model. A higher number density of precipitates is closely linked to a higher mean obstacle strength [11].

The evolution of the geometric slip distance, λ_g , in Fig. 11d) shows a slightly higher final value for the 0.5 % pre-stretched material. The precipitates in the material pre-stretched 4.0 % are then more effective to store GNDs. The evolution of the mean particle radius is shown in Fig. 11e) and confirms that the material pre-stretched 4.0 % has larger

particles than the material pre-stretched 0.5 %. Both the geometric slip distance and the mean particle radius are critical parameters for the evolution of the density of GNDs during final deformation and thus these parameters influence the work-hardening.

From Fig. 10 it is evident that the flow stress curves predicted by NaMo for AA6061–0.5% and AA6061–4.0% are quite similar. Since Fig. 11b) shows that the contribution from elements in solid solution is fairly similar for the two pre-stretched levels, the lower strength contribution from the precipitates in the 4.0 % pre-stretched materials must be compensated by the higher strength contribution from dislocations in the NaMo calculations, resulting in similar flow stress curves for the two pre-stretch levels.

The effect of the pre-stretching on work-hardening is discussed in terms of the dislocation densities. The evolution of ρ_s , ρ_g and ρ during the final deformation is shown in Fig. 12a) and the corresponding work-hardening in Fig. 12b) for both pre-stretching levels of AA6061. The plastic strain introduced by the 4.0 % pre-stretching has resulted in a high density of SSDs at the beginning of the final deformation. During artificial ageing, the static recovery was predicted by NaMo to be negligible for both pre-stretching levels, and thus the density of SSDs remains unchanged during artificial ageing. The increase in the dislocation densities during final deformation is markedly higher for the alloy pre-stretched 4.0 % than for the alloy pre-stretched 0.5 %, and at saturation the total dislocation density is about two times higher in the former. The reason for this is twofold. The higher density of SSDs after pre-stretching and artificial ageing, and the pinning of a major part of these on β' precipitates, imply that more SSDs are stored during the final deformation in the material pre-stretched 4.0 %. In addition, the geometrical slip distance is smaller in the 4.0 % pre-stretched material, which means that more GNDs are stored in this material during the final deformation. Even so, the work-hardening during the final deformation, calculated by Eq. (4), is higher for the 0.5 % pre-stretched material, as shown in Fig. 12b) for AA6061, because the 4.0 % pre-stretched material starts from a higher total dislocation density after pre-stretching and artificial ageing.

The hardening stagnation was not predicted in any of the NaMo-simulations, regardless of pre-stretch levels. For hardening stagnation to be predicted, the dislocation density must decrease in the beginning of the final deformation. To decrease the dislocation density, the dislocations generated during the pre-stretching must annihilate during deformation by dynamic recovery. To investigate this possibility, NaMo is modified so that all SSDs generated during pre-stretching are free to annihilate ($\phi = 0$) and the upper limit to the parameter controlling dynamic recovery (k_2) is removed. The simulations with these modifications are denoted “Case 2” in the following, while the original simulation is denoted “Case 1”. The hardening rate versus equivalent plastic strain and the evolution of the dislocation densities for AA6061–4.0%

are plotted in Fig. 13 for the two cases. As seen in Fig. 13a), marked work-hardening stagnation is present in Case 2 and the work-hardening rate is negative up to an equivalent plastic strain of about 0.025. This response is explained by the annihilation of SSDs occurring in the beginning of the deformation as shown in Fig. 13b). Contrary to Case 1, the density of SSDs continuously decreases in Case 2 for increasing plastic strain until saturation is reached. This results in a reduction in the total dislocation density, before it gently increases as the increase of the GNDs outweighs the decrease of the SSDs. The total dislocation density in Case 2 saturates at a level that is marginally lower than the initial value and much lower than in Case 1. This means that in Case 2, the material experiences only a small degree of work-hardening, which is not in agreement with the experimental results in Fig. 10a). It is possible that there exists a set of ϕ and k_2 values for which NaMo can predict a more reasonable yield plateau and the correct degree of work-hardening, but this possibility has not been investigated any further here.

The observations made in the TEM study by Qvale et al. [6] on the effect of pre-stretching on the microstructure, substantiate and confirm the predictions made by NaMo in this study. The TEM study investigated both undeformed and deformed samples where the characteristic parameters of the needle precipitates were measured and the interplay between the microstructural features was discussed. It was found that in the 4.0 % pre-stretched materials, precipitates nucleated along the generated dislocation lines in addition to the smaller precipitates that nucleated in the bulk. This resulted in a more inhomogeneous microstructure where the size of the precipitates varied within the material. Overall, a coarser microstructure was seen for the 4.0 % pre-stretched materials, which may be defined as an accelerated overageing. The superior ductility of the 4.0 % pre-stretched materials may stem from the coarse and inhomogeneous microstructure, which is typical in overaged alloys. Formation of dislocation cells was seen in the AA6063 profile pre-stretched 4.0 % after subsequent deformation and was attributed to the interaction between newly generated dislocations with the precipitates and the dislocations stemming from the pre-stretching. It should be noted that the formation of dislocation cells is not accounted for in the present version of NaMo. However, the increased length, cross-section and volume fraction and decreased number density of precipitates reported in Qvale et al. [6] for the materials pre-stretched 4.0 % compared to the ones pre-stretched 0.5 % are in agreement with the predictions by NaMo presented in Fig. 11.

The results from the tension tests in this study and the studies by Furu et al. [5] and Qvale et al. [6] suggest that the mechanical properties of 6xxx series aluminium alloys pre-stretched prior to artificial ageing are sensitive to both the chemical composition and the duration of the artificial ageing, as the effect of pre-stretching differs considerably for different alloy and temper combinations.

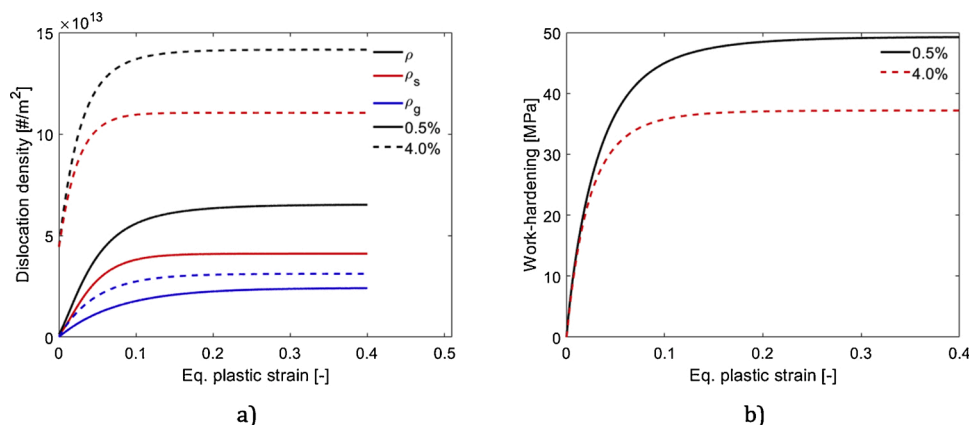


Fig. 12. a) Evolution of the total (ρ), statistically stored (ρ_s) and geometrically necessary (ρ_g) dislocation densities and b) the work-hardening of AA6061 pre-stretched 0.5 % and 4.0 % in the final deformation.

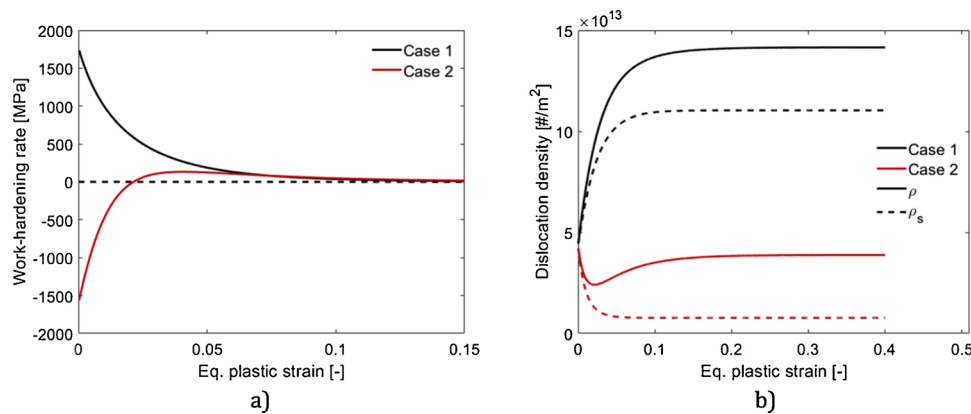


Fig. 13. a) Work-hardening rate versus equivalent plastic strain and b) the evolution of the total and statistically stored dislocation densities for two different simulations of AA6061-4.0 %. Case 1 is the reference case where ϕ is calculated according to Eq. (7) and an upper limit of $k_2 = 60$ is applied, whereas in Case 2, $\phi = 0$ and there is no upper limit for k_2 .

7. Concluding remarks

The effect of pre-stretching on the mechanical behaviour of three 6xxx series aluminium alloys has been investigated by experiments and nanostructure-based simulations. The uniaxial tension tests show that the alloys pre-stretched 4.0 % exhibit significantly better ductility than the alloys pre-stretched 0.5 %, without any prominent sacrifice in yield stress, work-hardening and ultimate tensile stress. The improved ductility is also evident in the crushing tests of the RHS profiles, where the alloys pre-stretched 4.0 % exhibit less cracks than those pre-stretched 0.5 % at a comparable energy absorption. The specific mean force in the crushing tests is less than 5 % lower for the alloys pre-stretched 4.0 %, suggesting that pre-stretching is an effective solution in energy absorption problems where crack initiation and propagation is the limiting factor.

The microstructure evolution simulated by NaMo indicates that the lower contribution from precipitates to the yield stress for the 4.0 % pre-stretched alloys is compensated for by the higher contribution from dislocations when compared to the 0.5 % pre-stretched alloys. The dislocations generated during pre-stretching have a slightly negative effect on the alloy's ability to work-harden. The accelerated precipitation kinetics seen for increasing pre-stretching levels suggests that the 4.0 % pre-stretched alloys tend towards an overaged condition, which is consistent with the observed increase in ductility.

Author statement

Henrik Granum: Writing – Original Draft, Visualization, Investigation, Formal analysis,

Ole Runar Myhr: Software, Conceptualization, Writing – Review & Editing

Tore Børvik: Conceptualization, Writing – Review & Editing, Supervision

Odd Sture Hopperstad: Conceptualization, Writing – Review & Editing, Supervision

Data availability

The raw/processed data required to reproduce these findings cannot be shared at this time due to technical or time limitations.

Declaration of Competing Interest

The authors declare that they have no known competing financial interests or personal relationships that could have appeared to influence the work reported in this paper.

Acknowledgments

The authors gratefully appreciate the financial support from NTNU and the Research Council of Norway through the FRINATEK Programme, Project No. 250553 (FractAl).

References

- [1] J. Hirsch, Recent development in aluminium for automotive applications, *Trans. Nonferrous Met. Soc. China* 24 (7) (2013) 1995–2002.
- [2] J. Zhu, T. Wierzbicki, W. Li, A review of safety-focused mechanical modeling of commercial lithium-ion batteries, *J. Power Sources* 378 (2018) 153–168.
- [3] I. Polmear, *Light Alloys: From Traditional Alloys to Nanocrystals*, 4th edition, Elsevier LTD, 2006.
- [4] J.G. Kaufman, *Introduction to Aluminium Alloys and Tempers*, ASM International, 2000.
- [5] Furu T., Ryen Ø, Myhr O. R. Effect of pre-deformation on age hardening kinetics in commercial 6xxx alloys. proceedings 11th International Conference on Aluminium Alloys (ICAA), September 2008, Aachen, Germany, Wiley-VCH, 1626-1633.
- [6] K. Qvale, O.S. Hopperstad, O. Reiso, U.H. Tundal, C.D. Marioara, T. Børvik, An experimental study on pre-strained double-chamber 6000-series aluminium profiles subjected to quasi-static and dynamic axial crushing, *Thin-walled Struct.* 158 (2021), 107160.
- [7] R. Abi-Akl, D. Mohr, Paint-bake effect on the plasticity and fracture of pre-strained aluminium 6451 sheets, *Int. J. Mech. Sci.* 124-125 (2017) 68–82.
- [8] Z. Wang, H. Li, F. Miao, B. Fang, R. Song, Z. Zheng, Improving the strength and ductility of Al-Mg-Si-Cu alloys by a novel thermo-mechanical treatment, *Mater. Sci. Eng. A* 607 (2014) 313–317.
- [9] R.O. Ritchie, The conflicts between strength and toughness, *Nat. Mater.* 10 (2011) 817–822.
- [10] O.R. Myhr, Ø. Grong, Modelling of non-isothermal transformations in alloys containing a particle distribution, *Acta Mater.* 48 (7) (2000) 1605–1615.
- [11] O.R. Myhr, Ø Grong, K.O. Pedersen, A combined precipitation, yield strength, and work hardening model for Al-Mg-Si alloys, *Metall. Mater. Trans. A* 41 (2010) 2276–2289.
- [12] O.R. Myhr, Ø Grong, C. Schäfer, An extended age-hardening model for Al-Mg-Si alloys incorporating the room-temperature storage and cold deformation process stages, *Metall. Mater. Trans. A* 46 (2015) 6018–6039.
- [13] O.R. Myhr, O.S. Hopperstad, T. Børvik, A combined precipitation, yield stress and work hardening model for Al-Mg-Si alloys incorporating the effects of strain rate and temperature, *Metall. Mater. Trans. A* 49 (2018) 3592–3609.
- [14] A. Simar, Y. Bréchet, B. de Meester, A. Denquin, T. Pardoën, Sequential modeling of local precipitation, strength and strain hardening of friction stir welds of an aluminium alloy 6005A-T6, *Acta Mater.* 55 (18) (2007) 6133–6143.
- [15] G. Fribourg, Y. Bréchet, A. Deschamps, A. Simar, Microstructure-based modelling of isotropic and kinematic strain hardening in precipitation-hardened aluminium alloy, *Acta Mater.* 59 (9) (2011) 3621–3635.
- [16] H. Granum, O.R. Myhr, T. Børvik, O.S. Hopperstad, Nanostructure-based finite element analyses of aluminium profiles subjected to quasi-static axial crushing, *Thin-walled Struct.* 131 (2018) 769–781.
- [17] eCorr User Manual. <https://www.ntnu.edu/kt/ecorr> [Accessed: 2020-08-05].
- [18] R. Wagner, R. Kampmann, Homogeneous second phase precipitation, in: R. W. Cahn, P. Haasen, E.J. Kramer (Eds.), *Materials Science and Technology: A Comprehensive Treatment*, VCH, Weinheim, Germany, 1991, pp. 213–303.
- [19] S. Thangaraju, M. Heilmaier, B.S. Murty, S.S. Vadlamani, On the estimation of true half-petch constants and their role on the superposition law exponent in Al alloys, *Adv. Eng. Mater.* 14 (10) (2012) 892–897.

- [20] K. Teichmann, C.D. Marioara, S.J. Andersen, K. Marthinsen, The effect of preaging deformation on the precipitatin behavior of an Al-Mg-Si alloy, *Metall. Mater. Trans. A* 43 (2012) 4006–4014.
- [21] K. Teichmann, C.D. Marioara, S.J. Andersen, K. Marthinsen, TEM study of β' precipitate interaction mechanisms with dislocations and β' interfaces with the aluminium matrix in Al-Mg-Si alloys, *Mater. Charact.* 75 (2013) 1–7.
- [22] K. Teichmann, C.D. Marioara, K.O. Pedersen, K. Marthinsen, The effect of simultaneous deformation and annealing on the precipitation behaviour and mechanical properties of an Al-Mg-Si alloy, *Mater. Sci. Eng. A* 565 (2013) 228–235.
- [23] E. Nes, Recovery revisited, *Acta Metall. Mater.* 43 (6) (1995) 2189–2207.
- [24] J.A. Sæter, B. Forbord, H.E. Vatne, E. Nes, Modelling recovery and recrystallization, applied to back-annealing of aluminium sheet alloys, in: *Proceedings of the 6th International Conference on Aluminium Alloys (ICAA6)*, Toyohasi, Japan, 5-10 July, 1998, pp. 113–126.
- [25] E. Nes, K. Marthinsen, Modeling the evolution in microstructure and properties during plastic deformation of f.c.c.-Metals and alloys – an approach towards a unified model, *Mater. Sci. Eng. A* 322 (1-2) (2002) 176–193.
- [26] O.R. Myhr, Ø Grong, S.J. Andersen, Modelling of the age hardening behaviour of Al-Mg-Si alloys, *Acta Mater.* 49 (1) (2001) 65–75.
- [27] O.R. Myhr, T. Børvik, C.D. Marioara, S. Wenner, O.S. Hopperstad, Nanoscale modelling of combined isotropic and kinematic hardening of 6000 series aluminium alloys, *Mech. Mater.* 151 (2020), 103603.